AIAA SciTech Forum
7-11 January 2019, San Diego, California
AIAA Scitech 2019 Forum
10.2514/6.2019-0608

# Aeroservoelastic Design and Wind Tunnel Testing using Parameter-Varying Optimal Control and Inertial-Based Sensing

Jeremy W. Hopwood*, Benjamin D. Ruskin†, David J. Broderick‡, and Fu-Shang (John) Wei§
*School of Engineering, Science, and Technology*
*Central Connecticut State University*
*New Britain, Connecticut 06050, USA*

**This research involved the formulation of a binary aeroservoelastic model, design and construction of the associated fixed angle-of-attack cantilever wing, the design of an optimal control system to suppress oscillations throughout the flight envelope, and the testing and analysis of the aeroservoelastic control system in the Central Connecticut State University wind tunnel. This research used oscillatory-unsteady aerodynamics, as opposed to a quasi-steady assumption, as well as a linear-quadratic regulator that was developed to minimize kinetic energy, elastic strain energy, and the input energy. In simulation, this controller displayed a good time response and continued stability past the flutter velocity. Furthermore, this research employed accelerometer/gyroscope state measurement, as opposed to strain-based sensing. Wind tunnel testing showed improved response at lower speeds, yet revealed parameter and delay sensitivity at high airspeeds.**

## I. Introduction

In aircraft design, it is often the goal to reduce weight and increase efficiency, while also increasing the flight envelope. However, such designs can experience the aeroelastic phenomenon of flutter - an unstable interaction between aerodynamic forces, structure elasticity, and inertial effects.[1,2] This interaction is largely due to the coupling between the change in lift due to bending and the change in lift due to torsion.[1] At a critical velocity, known as the flutter velocity, the structure will sustain the oscillations due to this coupling. At this point, the aerodynamic damping becomes zero. Past the flutter velocity, the damping becomes negative and the structure will experience unstable oscillation, leading to catastrophic failure. Traditionally, flutter, as well as aeroelastic oscillation in general, has been dealt with passively by improving wing design to eliminate this instability. This involves optimal mass placement in relation to the elastic axis and the aerodynamic center.[3–5] However, an active control system to bring aeroelastic stability can reduce weight and stiffness over traditional passive methods. This research involved *i)* the development of an aeroservoelastic model and associated wing design, *ii)* the design of an optimal control system to suppress oscillations throughout the flight envelope, and *iii)* the testing and analysis of the aeroservoelastic control system in the Central Connecticut State University wind tunnel.

*Undergraduate Student, Mechanical Engineering, CCSU, AIAA Student Member
†Undergraduate Student, Mechanical Engineering, CCSU, AIAA Student Member
‡Assistant Professor, Ph.D., Computer Electronics & Graphics Technology Department, CCSU, AIAA Member
§Associate Professor, D.Sc., Engineering Department, CCSU, AIAA/AHS Member

## II. Aeroservoelastic Model

To model the aeroservoelastic behavior, an assumed mode shape binary pitch-plunge aeroelastic model was used with a partial-span control surface as an input. Consider the symmetric airfoil pictured in Figure 1. The center of gravity (CG), or mass axis in the case of the three-dimensional wing, is positioned at a distance $x_m$ from the leading edge along the chord. Likewise, the elastic axis (EA) is positioned at a distance of $x_f$. The distance between the elastic axis and the aerodynamic center (AC) located at quarter-chord, $\varepsilon c$, is given by

$$\varepsilon c = x_f - \frac{c}{4} \tag{1}$$

where $\varepsilon$ is the eccentricity of the elastic axis about the aerodynamic center and $c$ is the chord length. The control surface hinges at an angle (positive downwards) of $\beta$. The frequency-dependent unsteady

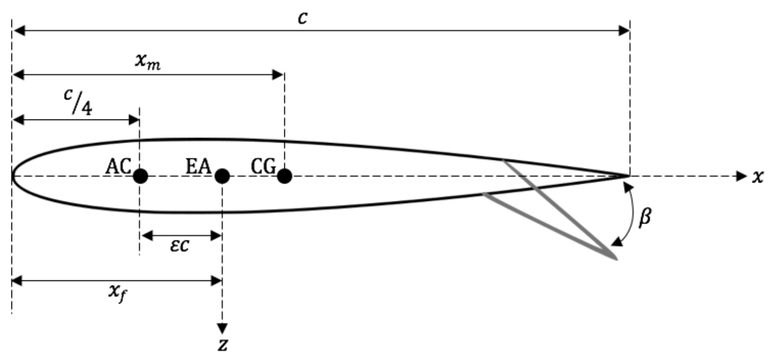


**Figure 1. Two-dimensional Airfoil with Control Flap**

aerodynamics were modeled using the Theodorsen function.[2,6] The unsteady aerodynamics exhibit both an attenuation and phase lag of the lift force of the wing, which are both a function of the dimensionless *reduced frequency*, $k$. The reduced frequency is defined as

$$k = \frac{\omega c}{2v} \tag{2}$$

where $\omega$ is the pitch oscillation frequency and $v$ is the flight velocity.[2] The Theodorsen function, $C(k)$, is given by

$$C(k) = F(k) + iG(k) = \frac{H_1^{(2)}(k)}{H_1^{(2)}(k) + iH_0^{(2)}(k)} \tag{3}$$

where $H_n^{(2)}(k)$ are the Hankel functions of the second kind. For the formulation of the unsteady aerodynamics, the motion of wing is assumed to be harmonic. Therefore, we have the relations

$$z = z_0 \mathrm{e}^{i\omega t} \tag{4a}$$

$$\dot{z} = i\omega\, z_0 \mathrm{e}^{i\omega t} \tag{4b}$$

$$\theta = \theta_0 \mathrm{e}^{i\omega t} \tag{4c}$$

$$\dot{\theta} = i\omega\, \theta_0 \mathrm{e}^{i\omega t} \tag{4d}$$

where $z$ and $\theta$ are the heave and pitch of the airfoil respectively, as shown in Figure 1. The unsteady lift and moment per unit span ($L'$ and $M'$), written in oscillatory aerodynamic derivative form, are expressed as[2]

$$L' = \rho v^2 b \left[ (L_z + ikL_{\dot{z}})\frac{z_0}{b} + (L_\theta + ikL_{\dot{\theta}})\theta_0 \right] \mathrm{e}^{i\omega t} \tag{5a}$$

$$M' = \rho v^2 b^2 \left[ (M_z + ikM_{\dot{z}})\frac{z_0}{b} + (M_\theta + ikM_{\dot{\theta}})\theta_0 \right] \mathrm{e}^{i\omega t} \tag{5b}$$

where $b$ is the semi-chord and $z_0$ and $\theta_0$ are the amplitudes of the heave and pitch oscillations of the airfoil. The oscillatory aerodynamic derivatives, as shown in Figure 2, are[2,6]

$$L_z = a_0 \left( -\frac{k^2}{2} - kG \right) \tag{6a}$$

$$L_{\dot{z}} = a_0 F \tag{6b}$$

$$L_\theta = a_0 \left[ \frac{k^2 a}{2} + F - kG\left(\frac{1}{2} - a\right) \right] \tag{6c}$$

$$L_{\dot{\theta}} = a_0 \left[ \frac{1}{2} + F\left(\frac{1}{2} - a\right) + \frac{G}{k} \right] \tag{6d}$$

$$M_z = a_0 \left[ -\frac{k^2 a}{2} - k\left(a + \frac{1}{2}\right) G \right] \tag{7a}$$

$$M_{\dot{z}} = a_0 \left(a + \frac{1}{2}\right) F \tag{7b}$$

$$M_\theta = a_0 \left[ \frac{k^2}{2}\left(\frac{1}{8} + a^2\right) + F\left(a + \frac{1}{2}\right) - kG\left(a + \frac{1}{2}\right)\left(\frac{1}{2} - a\right) \right] \tag{7c}$$

$$M_{\dot{\theta}} = a_0 \left[ -\frac{k}{2}\left(\frac{1}{2} - a\right) + kF\left(a + \frac{1}{2}\right)\left(\frac{1}{2} - a\right) + \frac{G}{k}\left(a + \frac{1}{2}\right) \right] \tag{7d}$$

where $a_0$ is the 2-D lift curve slope and

$$a = \frac{2x_f}{c} - 1 \tag{8}$$

Substituting Eq. (4) and Eq. (2) into Eq. (5), gives

$$L' = \rho v^2 \quad \left. L_z z + L_{\dot{z}}\frac{b\dot{z}}{v} + L_\theta b\theta + L_{\dot{\theta}}\frac{b^2\dot{\theta}}{v} \right) \tag{9a}$$

$$M' = \rho v^2 \quad \left. M_z bz + M_{\dot{z}}\frac{b^2\dot{z}}{v} + M_\theta b^2\theta + M_{\dot{\theta}}\frac{b^3\dot{\theta}}{v} \right) \tag{9b}$$

The elastic behavior of the wing was modeled with the assumption that there is no inertial coupling between bending and torsion as well as a uniform mass distribution. The heave and pitch of the wing are expressed in terms of the generalized bending and torsion coordinates, $q_b$ and $q_t$. The model only uses the first bending and torsion modes with the assumed shapes[2]

$$z(x, y, t) = \left(\frac{y}{s}\right)^2 q_b(t) + \left(\frac{y}{s}\right)(x - x_f)q_t(t) \tag{10a}$$

$$\theta(y, t) = \left(\frac{y}{s}\right) q_t(t) \tag{10b}$$

The elastic equations of motion are found using a Lagrangian approach with the wing's kinetic energy, $T_W$,

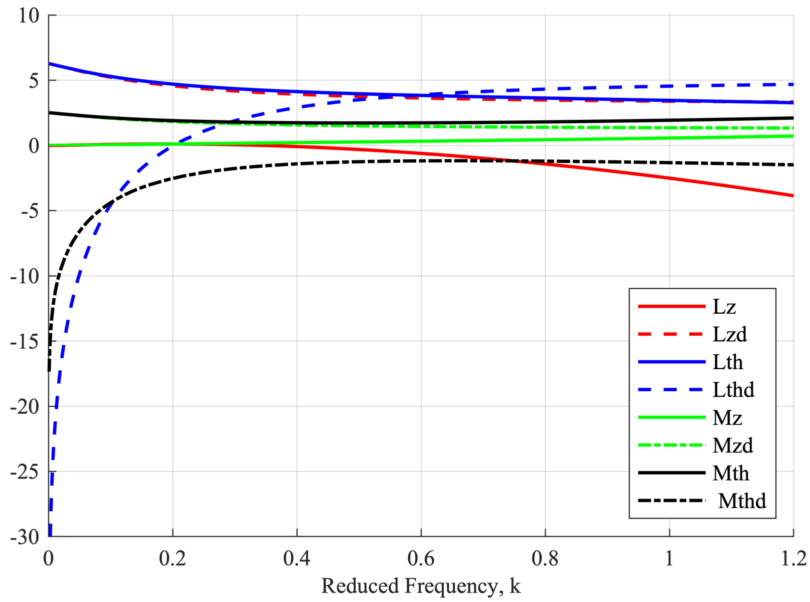


**Figure 2. Oscillatory Aerodynamic Derivatives**

and elastic potential energy, $U_W$, being[2]

$$T_W(x, y, t) = \frac{m}{2} \int_0^s \int_0^c \left[ \left(\frac{y}{s}\right)^2 \dot{q}_b(t) + \left(\frac{y}{s}\right)(x - x_f)\dot{q}_t(t) \right]^2 dx\, dy \tag{11}$$

$$U_W(y, t) = \frac{1}{2} \int_0^s \left[ EI \left(\frac{2q_b(t)}{s^2}\right)^2 + GJ \left(\frac{q_t(t)}{s}\right)^2 \right] dy \tag{12}$$

where $m$ is the mass per unit area, $EI$ is the bending rigidity, and $GJ$ is the torsional rigidity. Applying the Lagrange Equation yields the elastic model (no applied aerodynamic forces),

$$m \begin{bmatrix} \frac{sc}{5} & \frac{s}{4}\left(\frac{c^2}{2} - cx_f\right) \\ \frac{s}{4}\left(\frac{c^2}{2} - cx_f\right) & \frac{s}{3}\left(\frac{c^3}{3} - c^2 x_f + c x_f^2\right) \end{bmatrix} \begin{bmatrix} \ddot{q}_b \\ \ddot{q}_t \end{bmatrix} + \begin{bmatrix} \frac{4EI}{s^3} & 0 \\ 0 & \frac{GJ}{s} \end{bmatrix} \begin{bmatrix} q_b \\ q_t \end{bmatrix} = 0 \tag{13}$$

or

$$\mathbf{A\ddot{q}} + \mathbf{Eq} = \mathbf{0} \tag{14}$$

The aerodynamic forces acting on the wing are derived by simply integrating the lift and moment per unit span across the span. Also, the lift is assumed to vary elliptically across the span which is described by the wing lift curve slope:[7]

$$a_w = \frac{a_0}{1 + \frac{a_0}{\pi AR}} \tag{15}$$

where $AR$ is the aspect ratio. The elemental lift and moment are found substituting the definitions of the generalized coordinates from Eq. (10) into Eq. (9), yielding

$$dL = \rho v^2 \left( L_z(k)\frac{y^2}{s^2}q_b + L_\theta(k)\frac{cy}{2s}q_t \right) + \rho v \left( L_{\dot{z}}(k)\frac{cy^2}{2s^2}\dot{q}_b + L_{\dot{\theta}}(k)\frac{c^2 y}{4s}\dot{q}_t \right) \tag{16a}$$

$$dM = \rho v^2 \left( M_z(k)\frac{cy^2}{2s^2}q_b + M_\theta(k)\frac{c^2 y}{4s}q_t \right) + \rho v \left( M_{\dot{z}}(k)\frac{c^2 y^2}{4s^2}\dot{q}_b + M_{\dot{\theta}}(k)\frac{c^3 y}{8s}\dot{q}_t \right) \tag{16b}$$

The incremental work done on the wing by the aerodynamic forces is expressed as

$$\delta W = \int_0^s \left( -\frac{y^2}{s^2} dL \delta q_b + \frac{y}{s} dM \delta q_t \right) \tag{17}$$

Substituting the 2-D lift curve slope ($a_0$) for the wing lift slope described in Eq. (15) into the oscillatory aerodynamic derivatives, the generalized aerodynamic forces acting on the wing, $Q_{q_b}$ and $Q_{q_t}$, are formulated to be

$$Q_{q_b} = -\rho v^2 \left( L_z \frac{s}{5} q_b + L_\theta \frac{cs}{8} q_t + L_{\dot{z}} \frac{cs}{10v}\dot{q}_b + L_{\dot{\theta}} \frac{c^2 s}{16v}\dot{q}_t \right) \tag{18a}$$

$$Q_{q_t} = \rho v^2 \left( M_z \frac{cs}{8} q_b + M_\theta \frac{c^2 s}{12} q_t + M_{\dot{z}} \frac{c^2 s}{16v}\dot{q}_b + M_{\dot{\theta}} \frac{c^3 s}{24v}\dot{q}_t \right) \tag{18b}$$

Combining Eq. (18) with the elastic model described by Eq. (13), gives

$$m \begin{bmatrix} \frac{sc}{5} & \frac{s}{4}\left(\frac{c^2}{2} - cx_f\right) \\ \frac{s}{4}\left(\frac{c^2}{2} - cx_f\right) & \frac{s}{3}\left(\frac{c^3}{3} - c^2 x_f + cx_f^2\right) \end{bmatrix} \begin{bmatrix} \ddot{q}_b \\ \ddot{q}_t \end{bmatrix} + \rho v \begin{bmatrix} L_{\dot{z}}\frac{cs}{10} & L_{\dot{\theta}}\frac{c^2 s}{15} \\ -M_{\dot{z}}\frac{c^2 s}{16} & -M_{\dot{\theta}}\frac{c^3 s}{24} \end{bmatrix} \begin{bmatrix} \dot{q}_b \\ \dot{q}_t \end{bmatrix}$$
$$+ \left( \rho v^2 \begin{bmatrix} L_z \frac{s}{5} & L_\theta \frac{cs}{8} \\ -M_z \frac{cs}{8} & -M_\theta \frac{c^2 s}{12} \end{bmatrix} + \begin{bmatrix} \frac{4EI}{s^3} & 0 \\ 0 & \frac{GJ}{s} \end{bmatrix} \right) \begin{bmatrix} q_b \\ q_t \end{bmatrix} = 0 \tag{19}$$

or in matrix form,

$$\mathbf{A}\ddot{\mathbf{q}} + \rho v \mathbf{B}\dot{\mathbf{q}} + (\rho v^2 \mathbf{C} + \mathbf{E})\mathbf{q} = 0 \tag{20}$$

Now that the aeroelastic model has been formulated, the input of the control surface angle can be added to yield the full aeroservoelastic model. This model uses a partial-chord control surface, while neglecting its inertial effects and unsteady aerodynamics. The components of the elemental lift and moment attributed to the input are

$$dL_\beta = \frac{1}{2}\rho v^2 c a_\beta \beta dy \tag{21a}$$

$$dM_\beta = \frac{1}{2}\rho v^2 c^2 b_\beta \beta dy \tag{21b}$$

where the hinge coefficients are estimated as[2, 8]

$$a_\beta = \frac{a_w}{\pi}\left[\cos^{-1}(1 - 2\mathcal{E}) + 2\sqrt{\mathcal{E}(1-\mathcal{E})}\right] \tag{22a}$$

$$b_\beta = -\frac{a_w}{\pi}(1-\mathcal{E})\sqrt{\mathcal{E}(1-\mathcal{E})} \tag{22b}$$

where $\mathcal{E}$ is the fraction of the chord that is made up by the control surface. Applying the Lagrange equation to Eq. (21), integrating over the span of the control surface $[s_{ca}, s_{cb}]$, and combining with Eq. (19) results in the full unsteady model:

$$
m\begin{bmatrix} \frac{sc}{5} & \frac{s}{4}\left(\frac{c^2}{2}-cx_f\right) \\ \frac{s}{4}\left(\frac{c^2}{2}-cx_f\right) & \frac{s}{3}\left(\frac{c^3}{3}-c^2x_f+cx_f^2\right)\end{bmatrix}\begin{bmatrix}\ddot{q}_b \\ \ddot{q}_t\end{bmatrix}+\rho v\begin{bmatrix} L_{\dot{z}}\frac{cs}{10} & L_{\dot{\theta}}\frac{c^2s}{15} \\ -M_{\dot{z}}\frac{c^2s}{16} & -M_{\dot{\theta}}\frac{c^3s}{24}\end{bmatrix}\begin{bmatrix}\dot{q}_b \\ \dot{q}_t\end{bmatrix}
$$

$$
+\left(\rho v^2\begin{bmatrix} L_z\frac{s}{5} & L_\theta\frac{cs}{8} \\ -M_z\frac{cs}{8} & -M_\theta\frac{c^2s}{12}\end{bmatrix}+\begin{bmatrix}\frac{4EI}{s^3} & 0 \\ 0 & \frac{GJ}{s}\end{bmatrix}\right)\begin{bmatrix}q_b \\ q_t\end{bmatrix}=\rho v^2\begin{bmatrix}\frac{a_\beta c\left(s_{ca}^3-s_{cb}^3\right)}{6s^2} \\ -\frac{b_\beta c^2\left(s_{ca}^2-s_{cb}^2\right)}{4s}\end{bmatrix}\beta \quad (23)
$$

or in matrix form,

$$
\mathbf{A}\ddot{\mathbf{q}}+\rho v\mathbf{B}\dot{\mathbf{q}}+(\rho v^2\mathbf{C}+\mathbf{E})\mathbf{q}=\rho v^2\mathbf{g}\beta \quad (24)
$$

# III. System Design and Construction

## A. Wing Design

With the aeroservoelastic model developed, the physical wing was designed and fabricated. The wing was designed to be light and flexible, while still maintaining a primarily metal construction. This was done in order to reduce error due to viscoelastic effects as these effects can significantly alter the dynamics, especially at high frequencies, as such with this lightweight design.[9] The main structure of the wing was comprised of 6061-T6 aluminum sheet with an aluminum spar located at 45% chord to enforce the elastic axis location. The ribs were 3D printed and covered with a hobby aircraft skin to give the wing a NACA 0016 airfoil profile. A quarter-span, quarter-chord control flap was used, which was 3D printed with fiberglass reinforcement to maintain high stiffness (Figure 3). This flap was designed to be light and stiff in order to reduce modeling errors in neglecting the inertial effects of the control surface. It was directly coupled to a high-speed hobby servo motor, as there was ample torque for the deflections and airspeeds that were seen. The wing parameters are outlined in Table 1. The bending and torsional rigidity were calculated neglecting the ribs, skin, flap and servo. The torsion constant of the rectangular cross sections of the wing were estimated using Eq. (25), where $a$ is the length of the long side of the rectangle and $b$ is the the length of the short side.[10]

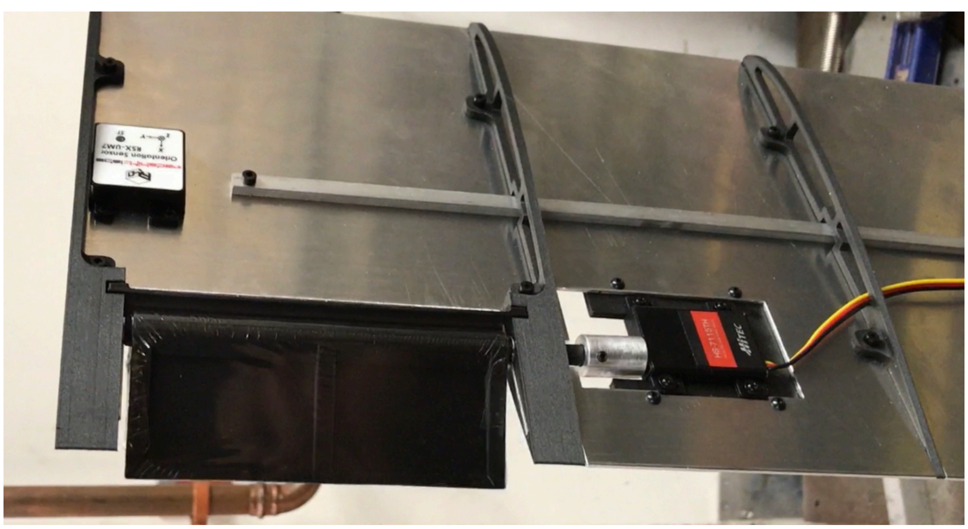

**Figure 3. Wing Construction**

$$J = ab^3\left(\frac{1}{3} - 0.21\frac{b}{a}\left(1 - \frac{b^4}{12a^4}\right)\right) \tag{25}$$

| Parameter | Nomenclature | Value | Units |
|---|---|---|---|
| Span | $s$ | 0.500 | m |
| Chord | $c$ | 0.200 | m |
| Mass per Unit Area | $m$ | 6.650 | $\mathrm{kg}/\mathrm{m}^2$ |
| Bending Rigidity | $EI$ | 22.68 | $\mathrm{Nm}^2$ |
| Torsional Rigidity | $GJ$ | 15.75 | $\mathrm{Nm}^2$ |
| Elastic Axis | $x_f$ | 0.090 | m |
| Control Surface Chord Fraction | $\mathcal{E}$ | 0.25 | $\mathrm{m}/\mathrm{m}$ |
| Control Surface Span-wise Location | $s_{ca} \leq y \leq s_{cb}$ | $0.375 \leq y \leq 0.500$ | m |

**Table 1. System Parameters**

### B. Electrical System

Commercially available electronics were used to implement the control system. A Redshift Labs UM7 Inertial Measurement Unit (IMU) with an extended Kalman filter was used to measure/estimate the angles and angular velocities at the tip of the wing placed on the elastic axis (Figure 3). This data was fed to a commercially available microcontroller via universal asynchronous receiver/transmitter serial communication (UART), where the states could be calculated using the assumed mode shapes. Also, a digital differential pressure sensor with a pitot tube was used to measure the difference in static and dynamic pressure in the wind tunnel, and therefore the airspeed. This can be seen in Figure 5. This sensor communicated with the microcontroller using an $I^2C$ serial interface. From the calculated states and the airspeed, the input to the servo was calculated. The IMU transmitted the desired data in binary packets at a user chosen 100 Hz with a serial BAUD rate of 115200. The control loop was executed as a packet was received (receive IMU packet $\rightarrow$ read pressure sensor $\rightarrow$ write to servo). This kept consistent timing and prevented bus overflow. Furthermore, it was desired that there be a way to input an impulse-like disturbance to the system during testing to excite the aeroelastic behavior at lower speeds. This was accomplished by having a real-time user input that, if triggered, would cause the servo to be written to a set disturbance angle (20°) and return to zero once the desired angle was reached.

### C. Wind Tunnel Testing Apparatus

The Central Connecticut State University wind tunnel used is an open return wind tunnel consisting a 2-ft × 2-ft test section (Figure 4). A slot was cut in the 1-inch thick acrylic window to accommodate the 10 cm excess of plate and spar. The rib at the root of the wing was positioned flush against the inside of the window (Figure 5). On the outside of the window, 90 degree steel was used to clamp the wing and then fix it to the window as seen in Figure 6. In addition, a catch net was installed in the case of structural failure of the wing (Figure 5). The wind tunnel is also fitted with a pitot tube and a hot-wire anemometer. Prior to testing, the control system's pitot tube was confirmed to be in agreement with the existing airspeed instrumentation.


**Figure 4. CCSU Wind Tunnel**

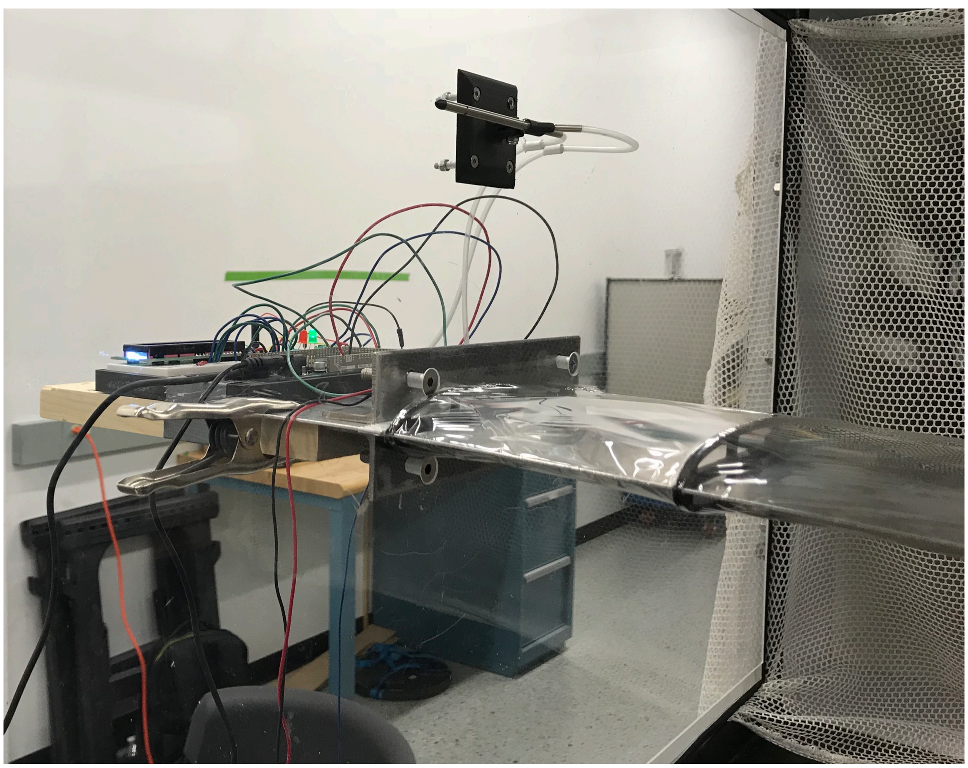

**Figure 5. Test Section**

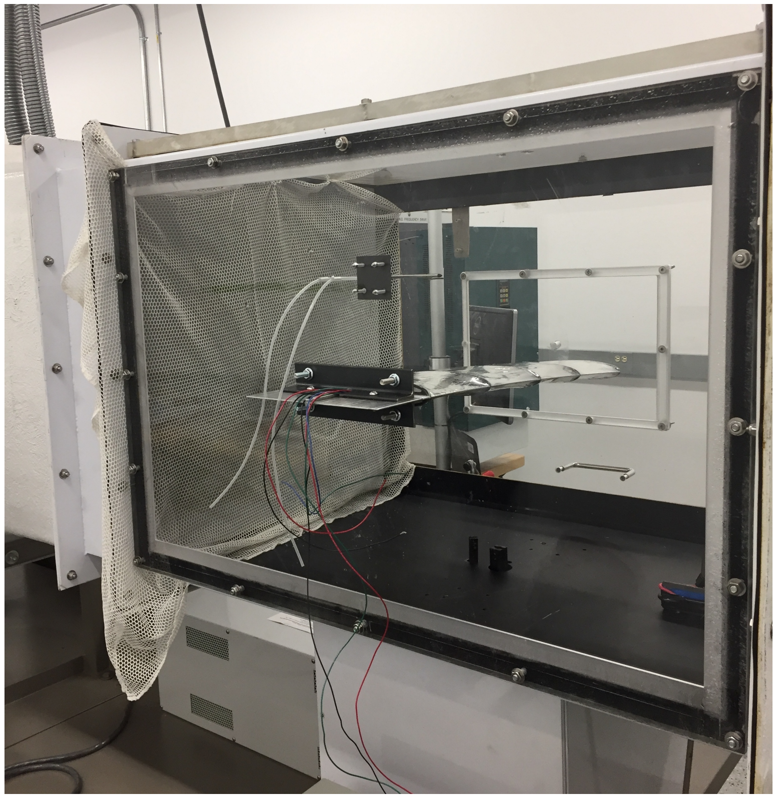

**Figure 6. Wing Mount**

# IV. Controller Design

With a wing designed and its parameters determined, the control system could be designed. In order to employ a state feedback control system, a state space model was formulated with states,

$$\mathbf{x}^\top = \begin{bmatrix} \mathbf{q} & \dot{\mathbf{q}} \end{bmatrix} = \begin{bmatrix} q_b & q_t & \dot{q}_b & \dot{q}_t \end{bmatrix} \tag{26}$$

The state space system is given as

$$\begin{bmatrix} \dot{\mathbf{q}} \\ \ddot{\mathbf{q}} \end{bmatrix} = \begin{bmatrix} 0 & \mathbf{I} \\ -\mathbf{A}^{-1}(\rho v^2 \mathbf{C} + \mathbf{E}) & -\mathbf{A}^{-1}(\rho v \mathbf{B}) \end{bmatrix} \begin{bmatrix} \mathbf{q} \\ \dot{\mathbf{q}} \end{bmatrix} + \begin{bmatrix} 0 \\ -\mathbf{A}^{-1}\mathbf{g} \end{bmatrix} \beta \tag{27}$$

or

$$\dot{\mathbf{x}} = \mathbf{A_s}\mathbf{x} + \mathbf{B_s}u \tag{28}$$

Now in first-order form, the eigenvalue solution form of the unforced aeroelastic system becomes[2,11]

$$(\mathbf{A_s} - \mathbf{I}\lambda)\mathbf{x} = 0 \tag{29}$$

The eigenvalues of the matrix $\mathbf{A_s}$ are in the form

$$\lambda = -\zeta\omega \pm i\omega\sqrt{1-\zeta^2} \tag{30}$$

where $\omega$ and $\zeta$ are the natural frequencies and damping ratios, respectively. This model is a function of reduced frequency, $k$, and the velocity, $v$. However, the relationship between these two variables can be found. The frequency used to calculate the oscillatory aerodynamic derivatives (and therefore, the state space matrices) is the unforced pitch frequency at each velocity.[2] This reduced frequency is found using the $p$-$k$ frequency matching method as follows:

**Algorithm 1:** $p$-$k$ frequency matching

```
initialize k_guess;
for v ← 0 to v_final do
    while k solution not converged do
        calculate aerodynamic matrices B and C using k_guess;
        calculate pitch frequency, ω, of system using Eq. (29);
        calculate k from pitch frequency;
        if solution converged then
            k_matched ← k;
        else
            k_guess ← k;
        end
    end
    k_guess ← k_matched;
end
```

With a reationship between $v$ and $k$ now established, the feedback matrix, $\mathbf{K}$, can be gain-scheduled by the velocity yielding the closed-loop system

$$\dot{\mathbf{x}}(t) = [\mathbf{A_s}(v) - \mathbf{B_s}(v)\mathbf{K}(v)]\,\mathbf{x}(t) \tag{31}$$

where

$$u = -\mathbf{Kx} \tag{32}$$

The state feedback matrix, $\mathbf{K}(v)$, was determined using linear-quadratic regulator (LQR) methods.[11,12] It is a necessary and sufficient condition that the system must be completely state controllable over the velocity range. The observability and controllability of the system were proved to be true for all velocities up through the divergence velocity. The LQR problem is such as to determine the optimal state feedback matrix, $\mathbf{K}$, as to minimize the cost functional,

$$J[x,u] = \int_0^\infty (\mathbf{x}^\top\mathbf{Q}\mathbf{x} + \mathbf{u}^\top\mathbf{R}\mathbf{u})\,dt \tag{33}$$

subject to dynamics, $\dot{\mathbf{x}} = \mathbf{A_s}\mathbf{x} + \mathbf{B_s}\mathbf{u}$ and state feedback, $\mathbf{u} = -\mathbf{Kx}$.

A multi-objective approach was used to determine the $\mathbf{Q}$ and $\mathbf{R}$ matrices. The first objective was to minimize the wing's kinetic energy. Evaluating Eq. (11), the coefficients of $\dot{q}_b$ and $\dot{q}_t$ were found to be 0.0665 and 0.000381, respectively. The second objective was to minimize the wing's elastic potential energy. Evaluating Eq. (12), the coefficients of $q_b$ and $q_t$ were found to be 362.90 and 15.754, respectively. The third objective was to reduce the magnitude of the control in order to stay within the physical constraints of the design (i.e. servo deflection, servo speed). In the case of a single input system, the $\mathbf{R}$ matrix becomes the scalar, $r$. Through simulation, this was arbitrarily chosen to have a value of 8 because this combination of $\mathbf{Q}$ and

$r$ showed good time response while staying within the physical limitations of the system. The $\mathbf{Q}$ matrix becomes

$$\mathbf{Q} = \begin{bmatrix} 362.90 & 0 & 0 & 0 \\ 0 & 15.754 & 0 & 0 \\ 0 & 0 & 0.0665 & 0 \\ 0 & 0 & 0 & 0.000381 \end{bmatrix} \tag{34}$$

With $\mathbf{Q}$ and $r$ determined, the state feedback matrix was found using the algebraic Riccati equation.[11,12] The gain was calculated at each integer velocity up to the divergence velocity.

## V. Model Analysis and Simulation

### A. Model Aeroelastic Analysis

With the parameters of the system determined, the aeroservoelastic system characteristics were then analyzed. The results of the $p$-$k$ frequency matching are shown in Figure 7. Furthermore, making use of

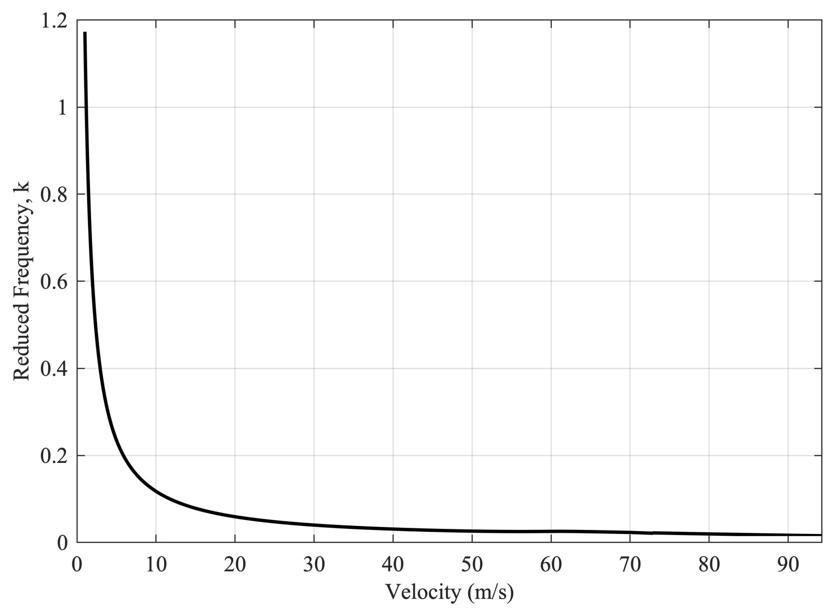


**Figure 7. Reduced Frequency by Velocity**

Eq. (30), the frequency and damping trends are shown in Figure 8. The flutter velocity is found at the point where the damping ratio becomes zero. The divergence velocity is found to be the velocity at which one of the system's eigenvalues becomes real, non-negative.[2] The corresponding flutter and divergence velocities are tabulated and presented in Table 2, as also seen in Figure 8. Furthermore, Figure 9 shows the path in

| Flutter Velocity | Divergence Velocity |
|---|---|
| 70.017 $\frac{\text{m}}{\text{s}}$ | 94.308 $\frac{\text{m}}{\text{s}}$ |

**Table 2. Flutter and Divergence Velocities**

the complex plane that the eigenvalues take as airspeed increases up to the divergence speed. Displayed are

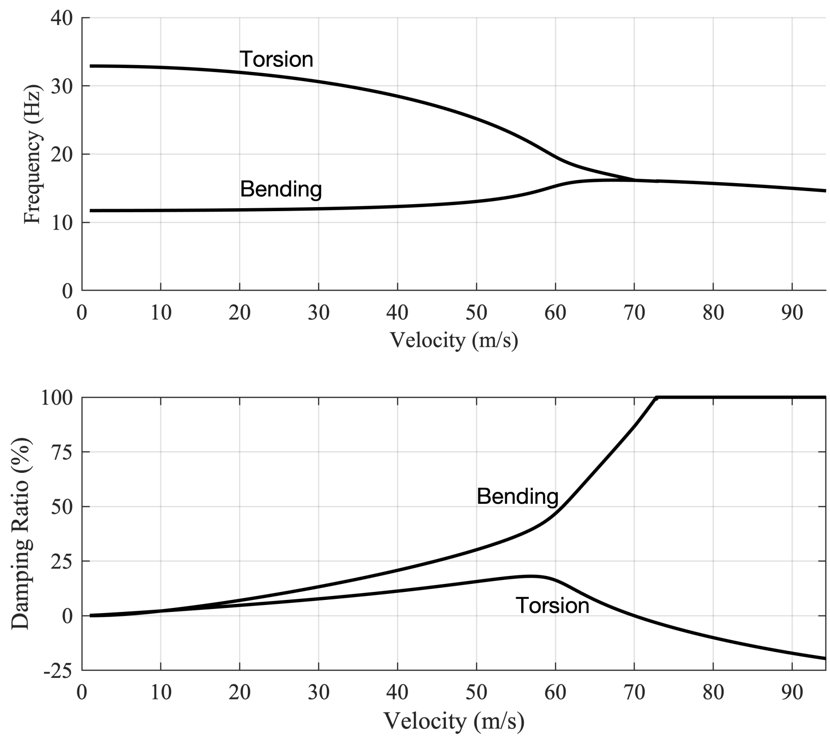


**Figure 8. Frequency and Damping Trends**

the eigenvalues for 50 $\frac{\text{m}}{\text{s}}$, 70.017 $\frac{\text{m}}{\text{s}}$ (Flutter Velocity), and 80 $\frac{\text{m}}{\text{s}}$ for reference.

## B. Open Loop Simulation

The open loop system response was simulated using Simulink™ subject to initial conditions,

$$\mathbf{x}_0^\top = \begin{bmatrix} 0 & 0 & 1 & 1 \end{bmatrix} \tag{35}$$

as zero is an equilibrium point of the system.[11,13] These initial conditions correspond to

$$\begin{aligned} \dot{z}(x_f, s, 0) &= 1\frac{\text{m}}{\text{s}} \\ \dot{\theta}(s, 0) &= 1\frac{\text{rad}}{\text{s}} \end{aligned} \tag{36}$$

These results are shown in Figure 10. As expected, there was decaying oscillation below the flutter speed (50 $\frac{\text{m}}{\text{s}}$), bounded oscillation exactly at the flutter speed (70.017 $\frac{\text{m}}{\text{s}}$), and exponential growth of oscillation above the flutter speed (80 $\frac{\text{m}}{\text{s}}$).

## C. Closed Loop Simulation

The closed loop system was simulated at the flutter velocity both with and without simulated state feedback noise. These results are shown in Figures 11 and 12. It can be seen that in simulation, the controller greatly

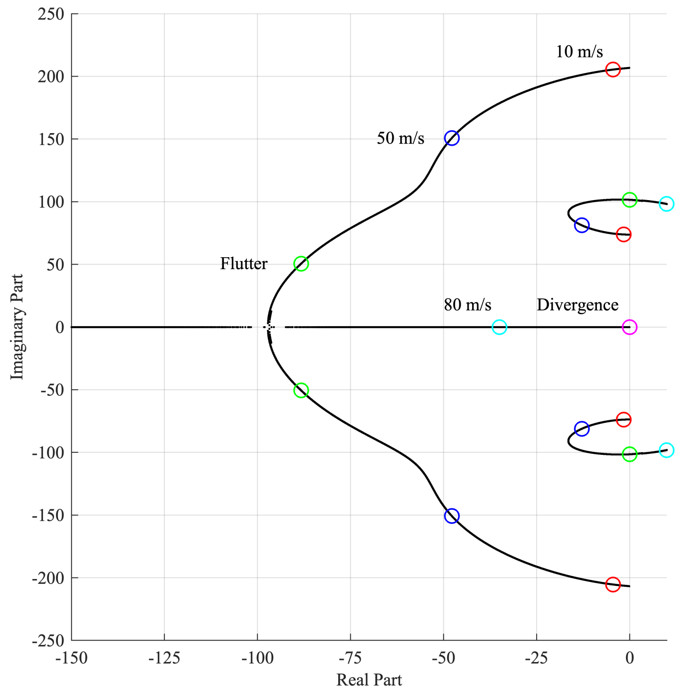


**Figure 9. Eigenvalues by Velocity**

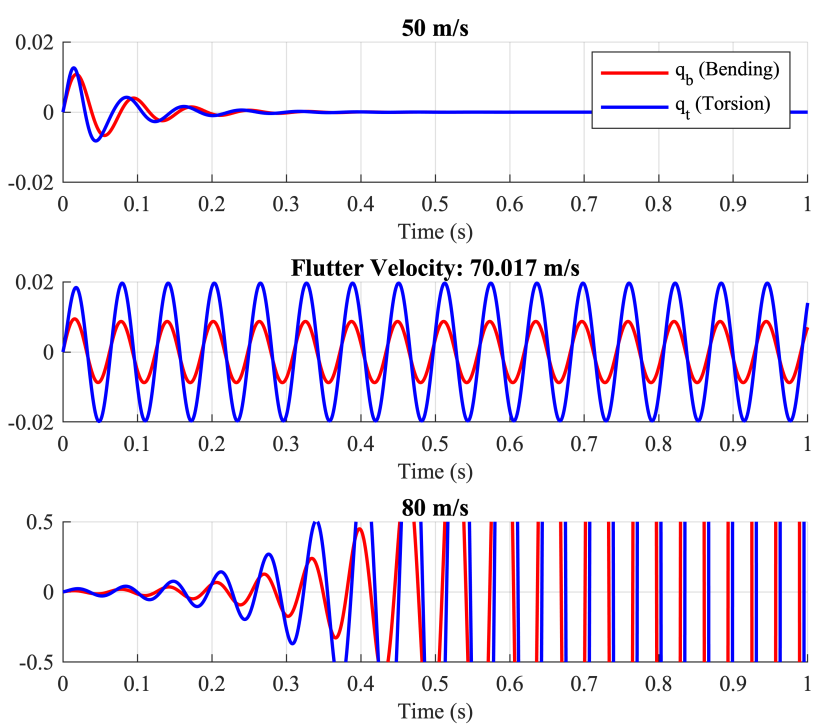


**Figure 10. Open Loop Response**

improved the response, even better so past the flutter velocity. It can also be seen that he controller rejects small error/noise in the measurement of the states, as closely shown in Figure 13. In addition to state feedback noise, non-linearities were added to the model, such as input saturation and input rate limiting. These values for these non-linearities were approximated from the published servo specifications. It can be seen that even with these physical limits, the response is still stable and well-damped.

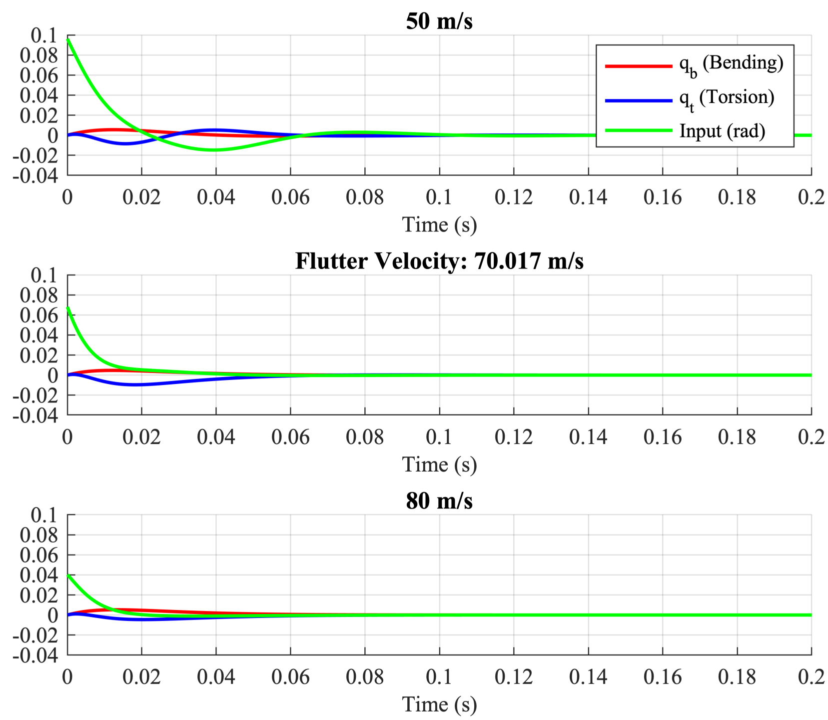


**Figure 11. Simulated LQR Controlled Response**

# VI. Wind Tunnel Test Results

Wind tunnel testing began with zero-airspeed testing to get the elastic frequencies of the wing and verify that the control system was running. Then, testing was conducted with small increases in velocity. Throughout each test, data was collected through serial communication from the microcontroller to a PC. For example one of these tests can be seen in Figure 14.

## A. Open Loop

Open loop data was collected by inputting three disturbances at various velocities up to just above the estimated flutter velocity. The zero airspeed bending response from an initial displacement is shown in Figure 15 along with the frequency spectrum of the the response, showing a distinct peak at 6.69 Hz. This test also yielded a torsional frequency of 28.0 Hz (not pictured). For the wind tunnel test, the 20° input disturbance response was analyzed at each velocity step up through 50 $\frac{m}{s}$. After 50 $\frac{m}{s}$, there was enough aerodynamic disturbance in the wind tunnel alone to excite sufficient bending and torsion to extract the

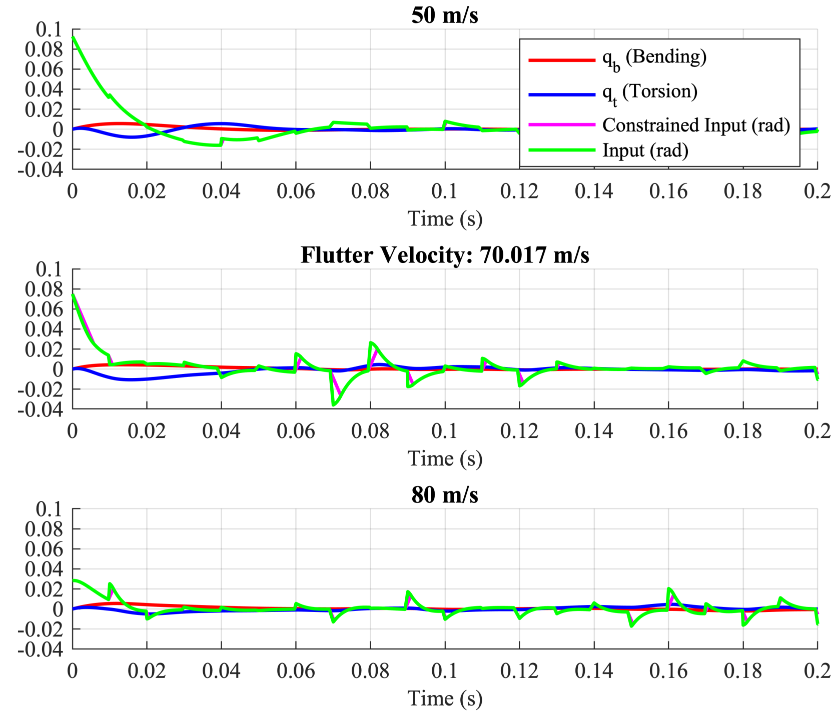


**Figure 12. Simulated LQR Controlled Response with State Feedback Noise**

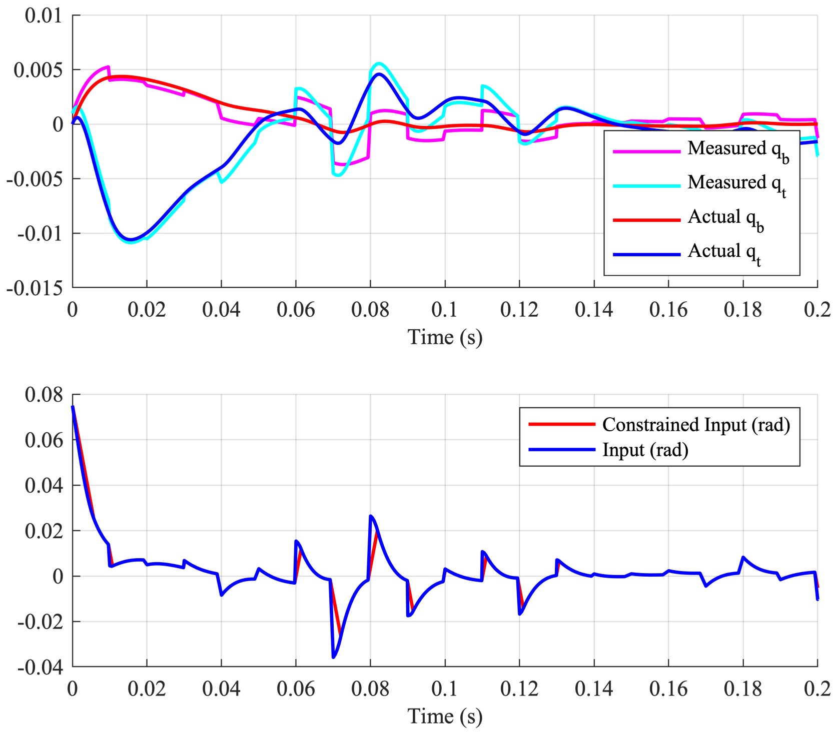


**Figure 13. Simulated LQR Control with Displayed State Feedback Noise**

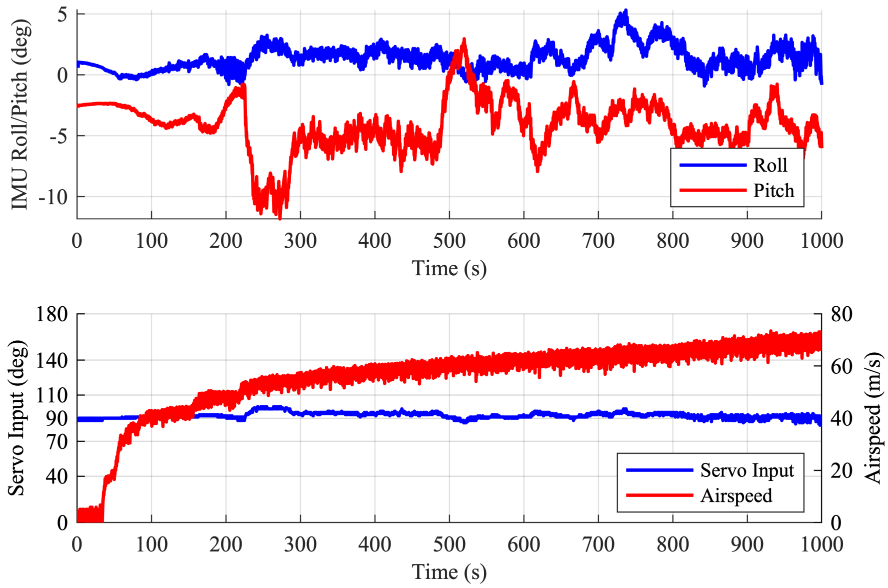


**Figure 14. Example of Full Test Data**

respective aeroelastic frequencies. The results of this frequency analysis are shown in Figure 16.

### B. Closed Loop

Closed loop data was collected in the same manner as the open loop data at approximately the same velocity steps. The calculated input was written to the servo as an integer value from 0 to 180, 90 being the zero position. With the 20 degree disturbance at low airspeeds with the control laws that were used, the calculated input to the servo was often smaller than the servo input resolution of 1 degree. The control laws do yield control flap movement that has a larger magnitude at a lower speed due to less aerodynamic forces on the control flap; however, the 20 degree control flap disturbance was not enough to significantly displace the wing at such airspeeds. One of the first velocities that control can be seen is at 40 $\frac{\mathrm{m}}{\mathrm{s}}$. This response, along with the open loop response at 40 $\frac{\mathrm{m}}{\mathrm{s}}$ is shown in Figure 17. Likewise, the open and closed loop response for airspeeds of 47 $\frac{\mathrm{m}}{\mathrm{s}}$, 60 $\frac{\mathrm{m}}{\mathrm{s}}$, and 72 $\frac{\mathrm{m}}{\mathrm{s}}$ can be seen in Figures 18, 19, and 20, respectively.

## VII. Discussion of Results

First, the zero airspeed data (Figure 15) showed distinct bending and torsion frequencies of 6.69 Hz and 28.0 Hz. However, the elastic model used yields bending and torsional frequencies of 11.73 Hz and 32.90 Hz respectively. This discrepancy was most likely due to the assumptions in calculating the bending and torsional rigidity, as the ribs and skin likely added significant rigidity. Despite this error, it is very straightforward to estimate the true bending and torsional rigidity through the data that was collected. Next, the open loop aeroelastic frequencies that were calculated loosely followed the trend of the theoretical plots; however, the bending and torsion frequencies do not couple as much at the calculated flutter velocity. Main sources of this difference include rigidity calculation error and lack of test repetition.

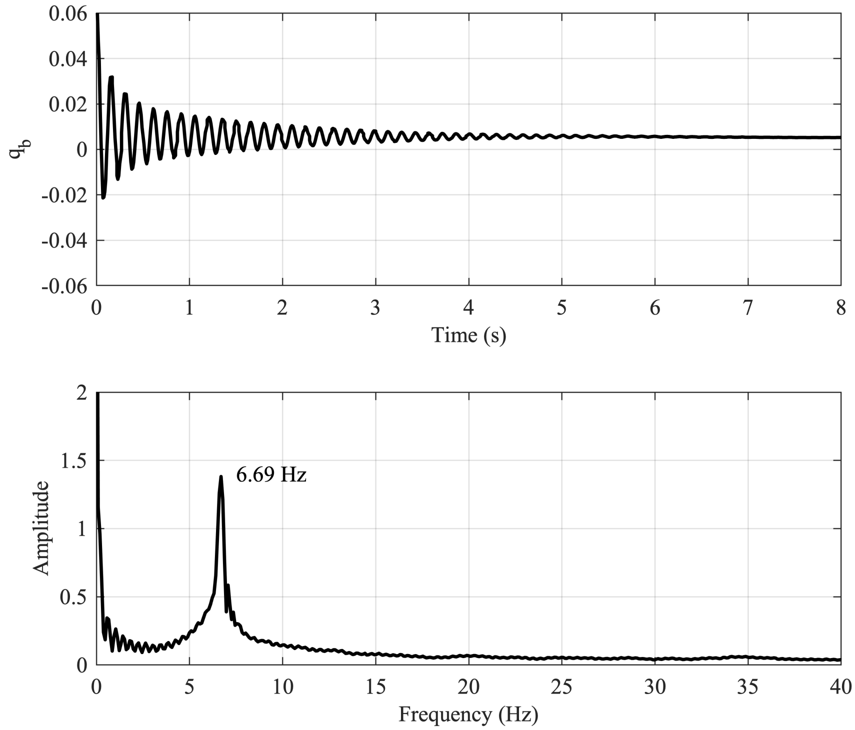


**Figure 15. Zero Airspeed Bending Response**

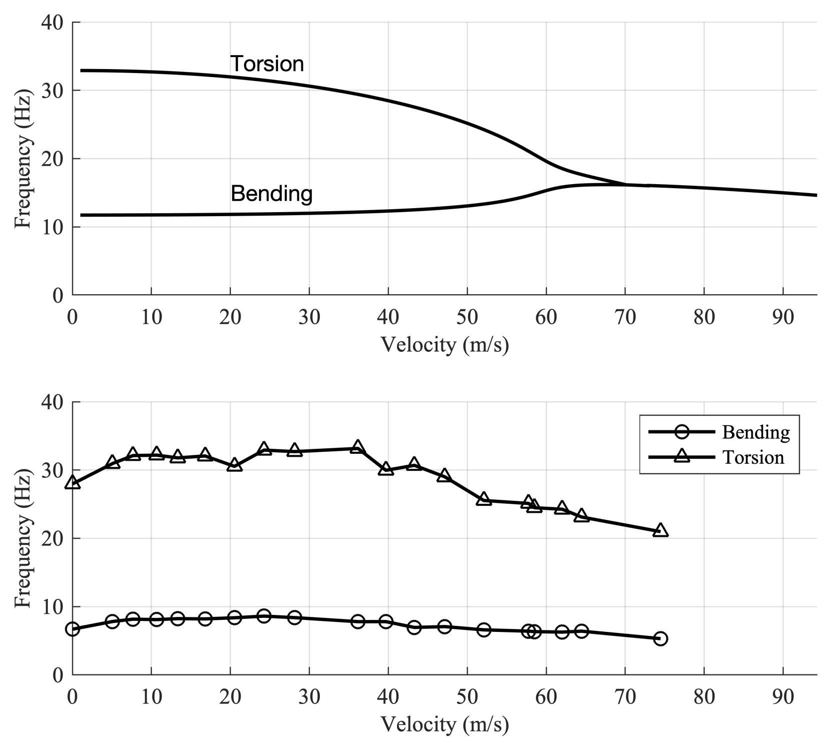


**Figure 16. Experimental Frequency Plot**

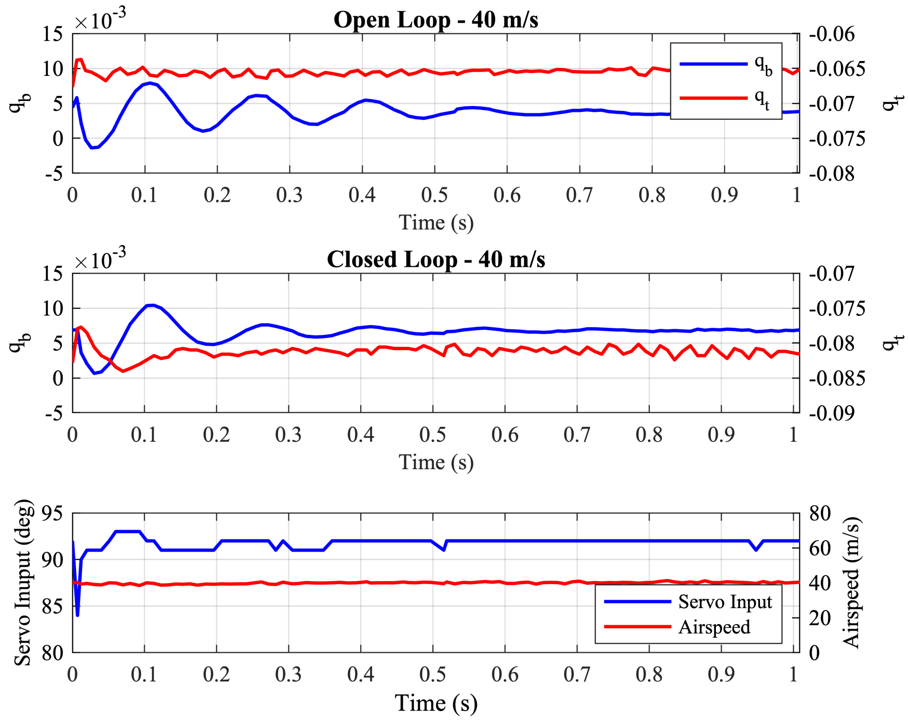


**Figure 17. 40 m/s Time Response**

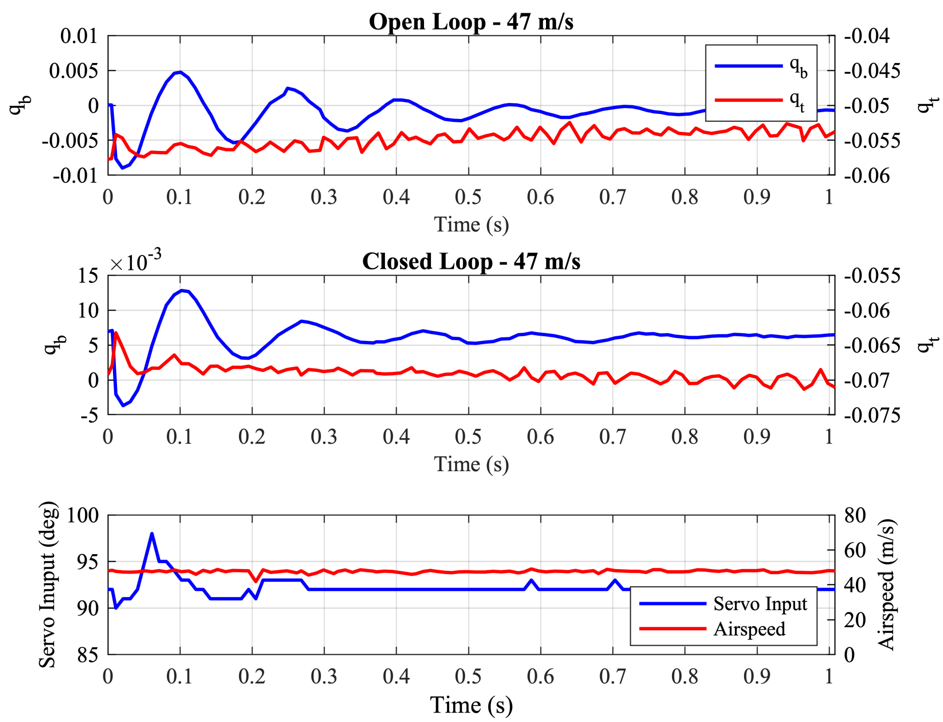


**Figure 18. 47 m/s Time Response**

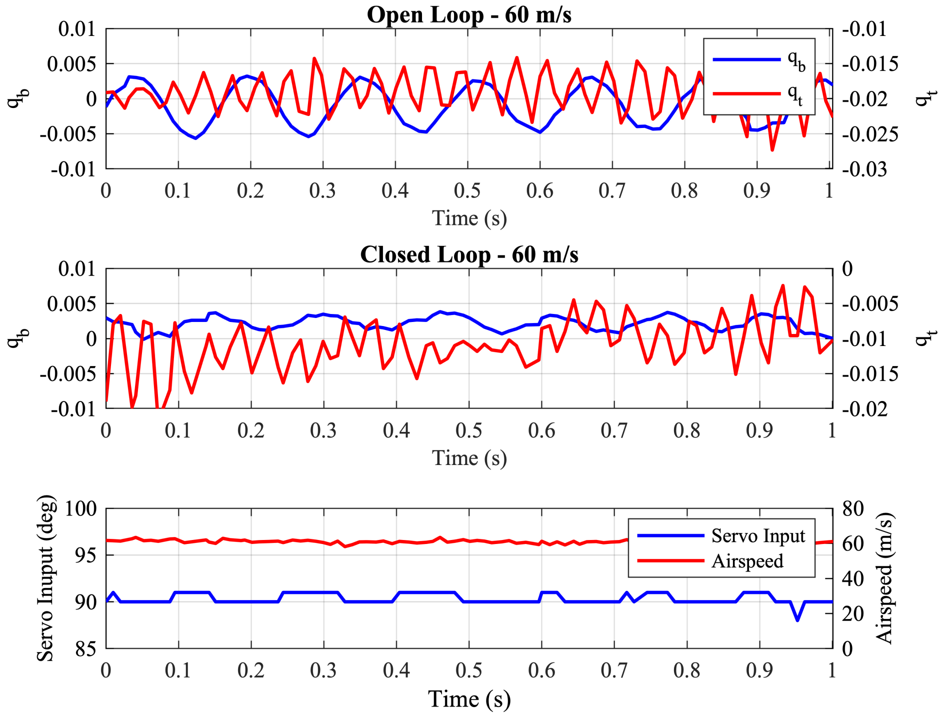


**Figure 19. 60 m/s Time Response**

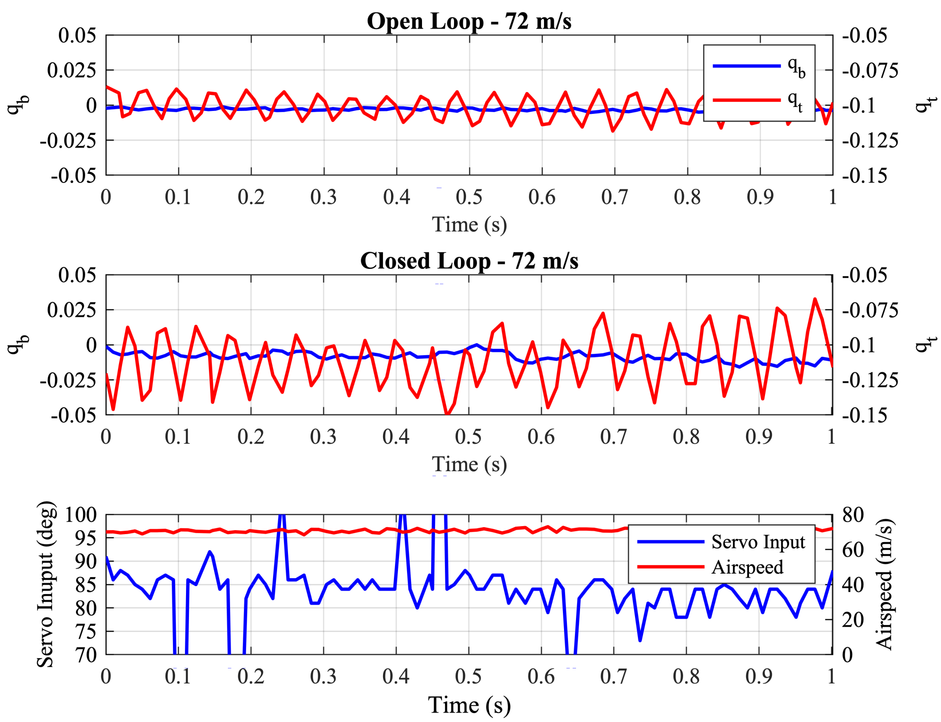


**Figure 20. 72 m/s Time Response**

Examining the closed loop data, shows an improved response at lower speeds; however, it is apparent that the controller actually increased the magnitude of oscillations at higher speeds (Figure 20). There are multiple possible contributions to this behavior. First, an error in $EI$ and $GJ$ can change the stability margin significantly and, therefore, the feedback gains of the system. Secondly, as evident in the results, the IMU's data rate was too slow for the frequencies that the wing was experiencing. The data is very non-smooth, especially with torsion. Thirdly, there was a measured 0.005 second delay, and due to the higher frequencies of the lightweight wing, this phase shift of the control could be enough to actually excite the wing.

Possible future work includes parameter estimation of system parameters, such as $EI$ and $GJ$, based on test data. Furthermore, this can also be accomplished using system identification methods in conjunction with testing.[14] Another technique would be to use on-line parameter estimation and use an adaptive control approach. In addition, the system delay can be approximated in the model used for designing the controller. Also, a more elegant optimal control solution with physical limitations as control solution bounds could yield a control solution that is tailored to the physical specifications of the servomotor/wing structure. Finally, these control methods and tests can be applied to more complex aeroservoelastic models including dynamic maneuvers, whole-aircraft modes and dynamics, greater number of included modes, and more sophisticated aerodynamic models.

## VIII. Conclusion

This paper presented the development of a binary aeroservoelastic model and associated wing design, the design of an optimal control system to suppress oscillations throughout the flight envelope, and the testing and analysis of the control system in the Central Connecticut State University wind tunnel. The linear-quadratic controller was designed with a multi-objective approach to minimize wing kinetic energy, elastic potential energy, and control energy. The controlled model was simulated and showed excellent time response. Furthermore, this research employed accelerometer/gyroscope state estimation, as opposed to strain-based sensing.[15–17] Testing did show a slightly improved response at lower speeds; however, the response at higher airspeeds was worse, yet still stable. A variety of factors were identified that may have caused this unwanted response, and possible solutions were discussed.

## Acknowledgments

This research was partially-funded by the NASA Connecticut Space Grant Consortium.

## References

[1]Bisplinghoff, R. L., Ashley, H., and Halfman, R. L., *Aeroelasticity*, Addison-Wesley Publishing Company, Inc., 1955.

[2]Wright, J. R. and Cooper, J. E., *Introduction to Aircraft Aeroelasticity and Loads*, John Wiley and Sons, Ltd, 2nd ed., 2015.

[3]Lang, G. F., "Diverging from the Mainstream with Heart Aflutter," *Sound and Vibration*, July 1992, pp. 4–5.

[4]Chambers, J. R., *Concept to Reality: Contributions of the NASA Langley Research Center to U.S. Civil Aircraft of the 1990s*, NASA history series, NASA Langley Research Center, 2003.

[5]Chambers, J. R., *Innovation In Flight: Research of the NASA Langley Research Center on revolutionary advanced concepts for aeronautics*, NASA Langley Research Center, 2005.

[6]Theodorsen, T., "General Theory of Aerodynamic Instability and the Mechanism of Flutter," Tech. rep., National Advisory Committee for Aeronautics, 1959.

[7]Glauert, H., *The Elements of Aerofoil and Airscrew Theory*, Cambridge University Press, 1926.

[8]Scanlan, R. H. and Rosenbaum, R., *Introduction To the Study of Aircraft Vibration and Flutter*, Macmillan, London, 1951.

[9]Merrett, C. and Hilton, H., "Generalized linear aero-servoviscoelasticity: theory and applications," *Proceedings 49thAIAA/ASME/ASCE/AHS structures, structural dynamics and materials conference, AIAA Paper AIAA-2008-1997*, AIAA Journal, Schaumburg, IL, 2014.

[10]Young, W. C., Budynas, R. G., and Sadegh, A. M., *Roark's Formulas for Stress and Strain*, McGraw-Hill, 2011.

[11]Ogata, K., *State Space Analysis of Control Systems*, Prentice-Hall, Inc., 1967.

[12]Lewis, F. L., Vrabie, D. L., and Syrmos, V. L., *Optimal Control*, John Wiley and Sons, Inc., 2012.

[13]Slotine, J.-J. E., *Applied Nonlinear Control*, Prentice-Hall, Inc., 1991.

[14]Broderick, D. J., Wei, F.-S., and Hopwood, J. W., "Controller Design and Validation of Dynamic Response for Full-Scale Helicopter Flight Simulator at CCSU," *Proceedings 2018 AIAA/ASCE/AHS/ASC Structures, Structural Dynamics, and Materials Conference*, 2017.

[15]Freydin, M., Rattner, M., and Raveh, D., "Strain-Based Aeroelastic Shape Sensing," *2018 AIAA/ASCE/AHS/ASC Structures, Structural Dynamics, and Materials Conference*, 2018.

[16]Chao, A., Changchuan, X., Yang, M., and Chao, Y., "Wind tunnel test and gust load alleviation of flexible wing including geometric nonlinearities with servo control," *2018 AIAA/ASCE/AHS/ASC Structures, Structural Dynamics, and Materials Conference*, 2018.

[17]Sutherland, A. N., *Aeroservoelastic Analysis, Design and Wind Tunnel Testing of a Three Degree-of-Freedom Binary Flutter Model*, Master's thesis, University of the Witwatersrand, 2011.